THE JOURNAL OF PHYSICAL CHEMISTRY LETTERS
A JOURNAL OF THE AMERICAN CHEMICAL SOCIETY

pubs.acs.org/JPCL

Letter

Ultra-incompressible High-Entropy Diborides

Xiaoliang Zhang, Weiwei Li, Hua Tian, Junxiu Liu, Cong Li, Hongliang Dong, Jian Chen, Meng Song, Bin Chen, Hongwei Sheng, Shanmin Wang, Dongzhou Zhang, and Hengzhong Zhang*

Cite This: *J. Phys. Chem. Lett.* 2021, 12, 3106–3113

Read Online

ACCESS | Metrics & More | Article Recommendations | Supporting Information

ABSTRACT: Transition metal borides are commonly hard and incompressible, offering great opportunities for advanced applications under extreme conditions. Recent studies show that the hardness of high-entropy borides may exceed that of their constituent simple borides due to the "cocktail effect". However, how high-entropy borides deform elastically remains largely unknown. Here, we show that two newly synthesized high-entropy diborides are ultra-incompressible, attaining ~90% of the incompressibility of single-crystalline diamond and exhibiting a 50−60% enhancement over the density functional theory predictions. This unusual behavior is attributed to a Hall−Petch-like effect resulting from nanosizing under high pressure, which increases the bulk moduli through dynamic dislocation interactions and creation of stacking faults. The exceptionally low compressibility, together with their high phase stabilities, high hardness, and high electric conductance, renders them promising candidates for electromechanics and microelectronic devices that demand strong resistance to environmental impacts, in addition to traditional grinding and abrading.

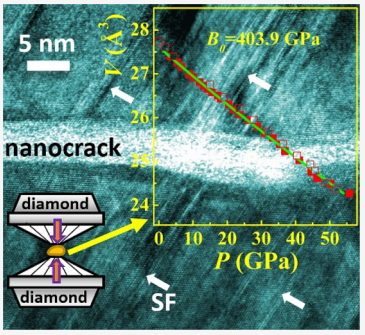

Many transition metal borides have high melting points, high hardness, high chemical stabilities, and good electric conductivities.[1−3] Thus, they have great potential for applications demanding exceptional mechanical performance and ultrahigh chemical stabilities, such as rock and mineral drill bits, tram and train wheels, wearing-resistant parts of microelectronic devices, and protecting layers of spacecrafts. With the successful synthesis of the first high-entropy oxide MgCoNiCuZnO$_5$,[4] other high-entropy compounds,[5−7] including high-entropy borides (HEBs),[8] emerged. Studies[8−13] showed that the hardness of HEBs is higher than the average hardness of their component borides due to the "cocktail effect".[14,15] For instance, $(Mo_{0.2}Zr_{0.2}Ta_{0.2}Nb_{0.2}Ti_{0.2})B_2$ has a Vickers hardness of 23.7 GPa, which is much higher than the average hardness (18.4 GPa) of its component diborides.[8] Thus, via a change in the chemical compositions of HEBs, it is possible to achieve optimal material properties and functions.

Although the plastic deformation of HEBs can be measured routinely (typically represented as the hardness), their elastic deformation behaviors remain largely unknown. In addition, lacking also is knowledge of their phase stabilities at high pressures, which is essential to their applications that include exposure to high degrees of impact and friction. Thus, in this work, we used synchrotron HP-XRD to study the compressibility and phase stabilities of two new HEBs: a quinary $(Ta_{0.2}Nb_{0.2}Zr_{0.2}Cr_{0.2}Ti_{0.2})B_2$ and a senary $(Ta_{0.167}Nb_{0.167}Zr_{0.167}Hf_{0.167}Ti_{0.167}Cr_{0.167})B_2$. We found that both HEBs are ultra-incompressible (bulk moduli of ~400 GPa), and both are structurally stable at pressures of $\lesssim$50 GPa. These outstanding features make them excellent candidates for applications requiring extremely high mechanical performance.

The two new HEB samples were synthesized using the spark plasma sintering (SPS) method (details of the synthesis in the Supporting Information). Their XRD patterns match that of a hexagonal structure quite well (Figure 1a,b),[16] indicating that the two synthesized samples were single phases. Rietveld fitting (Figure 1a,b) of the XRD patterns gave the lattice parameters of a hexagonal structure (space group *P6/mmm*): for the quinary HEB, a = 3.100 ± 0.001 Å and c = 3.336 ± 0.002 Å, and for the senary HEB, a = 3.094 ± 0.001 Å and c = 3.346 ± 0.001 Å. Scanning electron microscopy (SEM) images of the two samples (Figure 1c,d) show that there is no phase segregation. Some voids/pores can be seen in the samples, which might form due to the volume contractions of the reactants during the syntheses. Elemental mapping using energy dispersive X-ray spectroscopy (EDS) shows that the transition metal elements are distributed evenly in the samples (Figure S1a,b). Their compositions determined via EDS (Figure S1c,d) and X-ray fluorescence (XRF) are virtually equivalent, though they deviate somewhat from the nominal values (Table S1) possibly due to the minor and unequal sublimations of the metal elements during the syntheses.

Both the Vickers hardness (H_v) and the nanoindentation (NIT) hardness (H_{NIT}) of the synthesized HEBs were measured. The results are listed in Table S2 together with

Received: February 3, 2021
Accepted: March 16, 2021
Published: March 23, 2021

https://doi.org/10.1021/acs.jpclett.1c00399
J. Phys. Chem. Lett. 2021, 12, 3106–3113

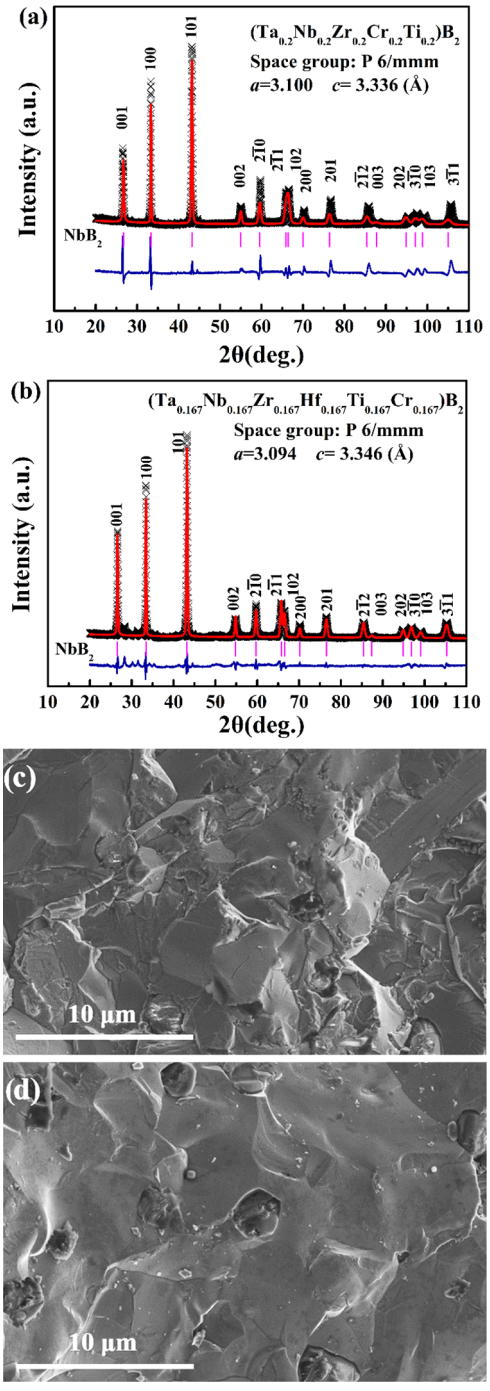

Figure 1. Ambient XRD patterns of (a) quinary HEB $(Ta_{0.2}Nb_{0.2}Zr_{0.2}Cr_{0.2}Ti_{0.2})B_2$ and (b) senary HEB $(Ta_{0.167}Nb_{0.167}Zr_{0.167}Hf_{0.167}Ti_{0.167}Cr_{0.167})B_2$. (c) SEM image of the quinary HEB. (d) SEM image of the senary HEB. In panels a and b, black lines denote experimental data, red lines Rietveld fitting, blue lines differences between the data and the fittings, and pink lines peak positions with various indices from ref 16. The X-ray wavelength is 1.54056 Å.

literature values of their constituent simple diborides.[1,2] Due to the existence of voids/pores in the samples, some measurements underestimated the H_v values of the HEBs, especially the senary HEB. By referring to the average H_v of their constituent simple diborides (Table S2), we infer that the H_v values of the HEBs measured at a 2.0 N loading (~28 GPa for the quinary and ~24 GPa for the senary) are close to the true values. As nanoindentation can largely avoid indenting on sample voids/pores, H_{NIT} should be more intrinsic to the HEBs. Multiple nanoindentation tests were conducted to reduce the statistical errors (Tables S3 and S4). The results (Table S2) show that the H_{NIT} of the quinary HEB is 37.5 GPa, apparently higher than the average value of its constituent diborides (32.0 GPa), while that of the senary HEB is 32.2 GPa, close to the average value of its constituent diborides (32.6 GPa). Their H_{NIT}/H_v ratio (~1.34) is comparable to a previously reported value (1.25[17]). The measured Young's modulus (E) of the quinary HEB is significantly higher than the average value of the constituent diborides (Table S2). Thus, the "cocktail effect"[14,15] is more obvious in the quinary HEB than in the senary one.

Synchrotron in situ HP-XRD was used to study the phase stabilities and the elastic deformation behaviors of the two new HEBs. A diamond anvil cell (DAC) was used to generate high pressures on a HEB sample.[18] HP-XRD patterns of the quinary and senary HEBs are shown in Figure 2a–d. For the quinary HEB (Figure 2a), the XRD pattern at the initial pressure (0.9 GPa) is consistent with that at ambient pressure (Figure 1a). However, from ~0.9 to ~15.1 GPa, the (001) peak is quite weak, possibly due to a preferred orientation of the sample crystallites whose (001) planes are mostly parallel to the diamond culet surface. This is proved by examining the original XRD image as shown in Figure S2a (at 9.8 GPa). One can see that there are barely diffraction rings or spots from the (001) and (002) planes. This indicates that, under compression, the relatively large sample grains produced by manual grinding tended to orient collectively such that their hexagonal stacking planes inclined to lay down on the diamond culet surface. As a result, no (or rare) diffraction from these planes could be produced.

When the pressure was increased to ~18 GPa, the (001) peak intensity began to increase (Figure 2a). This can be attributed to the formation of nanocrystallites through nanocracking and then grain rotation while under HP compression.[19,20] This is supported by the original XRD images like the one at 52.7 GPa (Figure S2b), which shows that there are obvious diffraction rings from the (001) and (002) planes. In comparison, the (001) and (002) peaks of the senary HEB are more apparent (Figure 2c,d and Figure S2c,d), because the sample was rotating during the XRD measurements to reduce the adverse effect of the preferred orientation on the diffraction intensity (see the Supporting Information).

Under compression of the quinary sample up to 52.7 GPa (Figure 2a) and subsequent decompression to 0.3 GPa (Figure 2b), no new peaks appeared and no existing peaks disappeared. This indicates that the quinary HEB experienced no phase transition and hence is structurally stable at pressures of $\lesssim$53 GPa. A similar conclusion also holds for the senary HEB at pressures of $\lesssim$56 GPa, as seen from its HP-XRD patterns in panels c and d of Figure 2.

XRD line profile fitting was used to deduce accurate XRD peak positions and peak widths. Then, lattice parameters of the HEBs (Tables S5 and S6) as a function of pressure were derived from the positions of the (001), (100), (101), (21(—)0), (200), and (201) peaks based on the relationship between the lattice spacing and the cell parameters.[21] The following third-order Birch–Murnaghan equation of state (EOS) was used to fit the variation of the unit cell volume (V) with pressure (P):[22]

https://doi.org/10.1021/acs.jpclett.1c00399
J. Phys. Chem. Lett. 2021, 12, 3106–3113

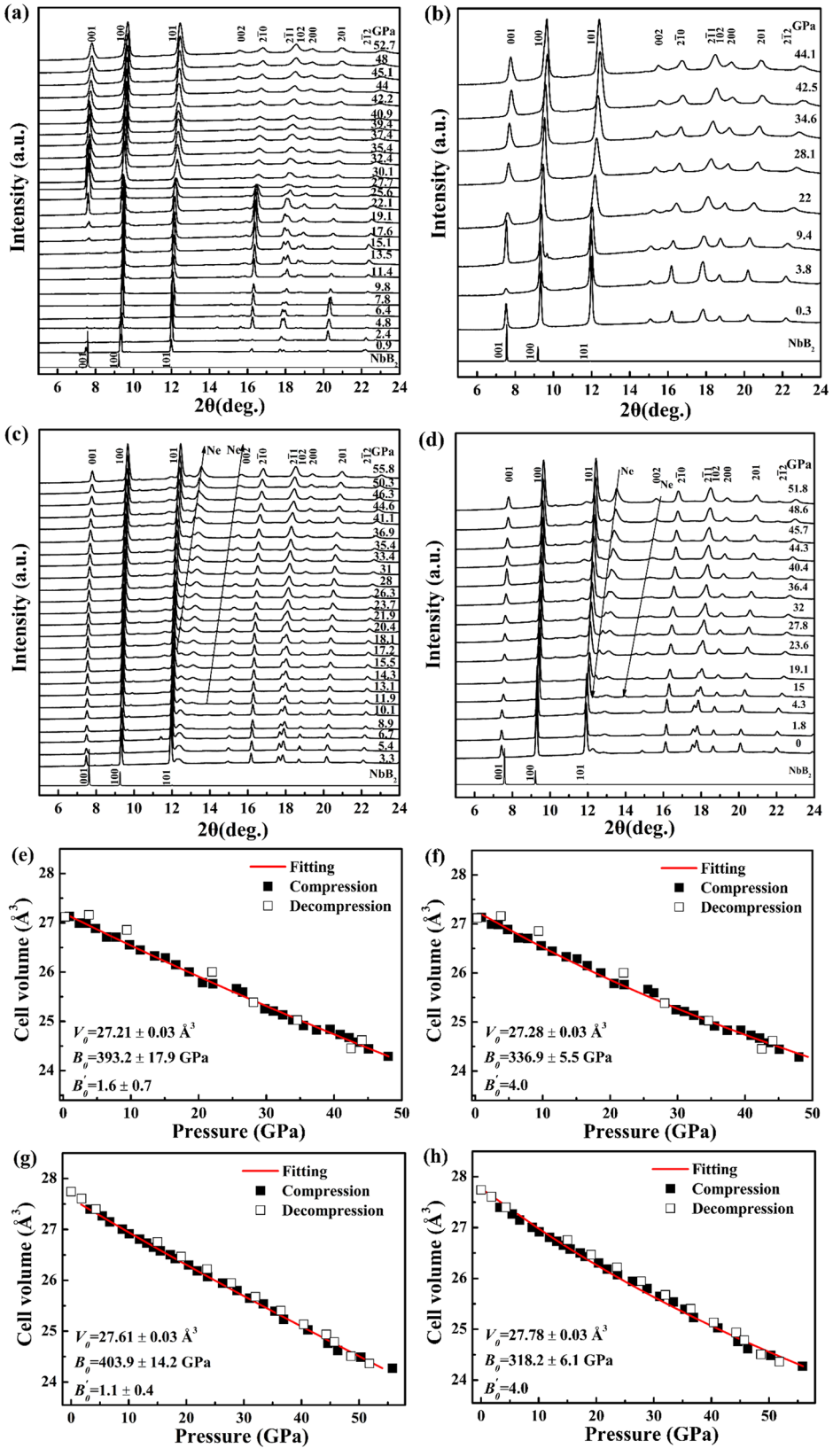

Figure 2. High-pressure XRD patterns of the quinary HEB sample under (a) compression and (b) decompression with silicone oil as the pressure-transmitting medium. High-pressure XRD patterns of the senary HEB sample under (c) compression and (d) decompression with neon as the pressure-transmitting medium. The calculated XRD pattern of hexagonal NbB_2 (using a CIF file from ref 29) is included at the bottom of each diagram for comparison. The X-ray wavelength is 0.4335 Å. Pressure dependence of the unit cell volume of the quinary HEB and its EOS fitting with (e) a fitted B_0' and (f) a fixed B_0' of 4. Pressure dependence of the unit cell volume of the senary HEB and the EOS fitting with (g) a fitted B_0' and (h) a fixed B_0' of 4. Standard errors of all determined unit cell volumes are within 0.02 Å^3.

https://doi.org/10.1021/acs.jpclett.1c00399
J. Phys. Chem. Lett. 2021, 12, 3106−3113

$$P(V) = 1.5B_0\left[\left(\frac{V_0}{V}\right)^{7/3} - \left(\frac{V_0}{V}\right)^{5/3}\right]\left\{1 + \frac{3}{4}(B_0' - 4)\left[\left(\frac{V_0}{V}\right)^{2/3} - 1\right]\right\} \quad (1)$$

where B_0, B_0', and V_0 are the bulk modulus, its pressure derivative, and the unit cell volume at ambient pressure, respectively. For most bulk materials under hydrostatic compression, B_0' is commonly fixed at 4.0 in fitting.[23] However, tests showed that fitting of the unit cell volumes of the HEBs with a variable B_0' produced a much lower residual than constraining B_0' to 4.0 (e.g., for the senary HEB with and without fixing B_0' to 4.0, the corresponding residual sums of squares are 27.61 and 10.24 Å^6, respectively). In addition, as shown in Figure S3, the trend lines describing the variations of the normalized pressures versus the Eulerian strains for the two HEBs are slanted (nonhorizontal), further confirming their B_0' values are not equal to 4.0.[24]

Figure 2e−h shows the EOS fitting. For the quinary HEB, the derived bulk moduli are B_0 = 393.2 ± 17.9 GPa with a fitted B_0' of 1.6 ± 0.7 and B_0 = 336.9 ± 5.5 GPa if one sets B_0' to 4. For the senary HEB, the derived bulk moduli are B_0 = 403.9 ± 14.2 GPa with a fitted B_0' of 1.1 ± 0.4 and B_0 = 318.2 ± 6.1 GPa if one sets B_0' to 4. It is surprising to see that the bulk moduli of the two HEBs are extremely high (∼400 GPa) when using a variable B_0', which are ∼90% of the B_0 of a single-crystal diamond (443 GPa[25]) and are apparently higher than that of superhard nanocrystalline cubic BN (375 GPa at B_0' = 2.3).[26] Due to these facts, the two HEBs can be classified as ultra-incompressible, just as the OsB_2 compound whose B_0 = 395 GPa (B_0' = 1.4).[27] Even if with a fixed B_0' of 4, the bulk moduli of the two HEBs are still comparable to that of the high-pressure phase TiO_2−OII whose B_0 = 312 GPa.[28] For these ultra-incompressible HEBs, the difference between the hydrostaticity of the used silicone oil (for the quinary HEB) and the neon pressure medium (for the senary HEB) becomes insignificant. Thus, the large deviation of the fitted B_0' (1.1−1.6) from the common value of 4.0 for bulk materials indicates that these HEB materials exhibit compression behaviors that are different from those of most bulk materials.

We conducted extensive density functional theory (DFT) calculations of the compressibilities of the HEBs, attempting to rationalize their measured extremely high bulk moduli. First, the bulk moduli of a series of simple diborides were calculated to gauge the computational methods (Table S7) (details of the calculations are available in the Supporting Information). The root-mean squares (RMS) of the differences between the DFT predictions and the experiments are similar for all computations (RMS ranging from ∼20 to 27 GPa). This indicates that all computational methods, including CASTEP,[30] CP2K,[31] and Quantum ESPRESSO,[32] used in this work and those in the literatures[2,33,34] are comparable. Excluding WB_2, OsB_2, and ReB_2, we found that the average computed bulk moduli agree with the average experimental ones within a deviation of 20 GPa, confirming the reliability of the DFT calculations. On this basis, the averaged DFT-predicted bulk moduli of the quinary and senary HEBs, 257 and 254 GPa, respectively (Table S7), should be close to the true B_0 values of bulk crystallites of the HEBs. However, the experimentally determined B_0 values, 393 GPa for the quinary HEB and 404 GPa for the senary HEB (with a fitted B_0'), are approximately 50−60% higher than the DFT-predicted values. We infer that the Hall−Petch-like (HPL) effect[35−37] known to increase the incompressibility of nanocrystallites accounts for the exceptionally high B_0 of the HEBs.

We used SEM and transmission electron microscopy (TEM) to examine the morphologies and crystallite sizes of the two HEB samples quenched from compression to ∼55 GPa in a DAC. SEM images (Figure 3a and Figure S4) show the quinary samples cracked to form nano- to micrometer-sized grains at this high pressure. TEM images (Figure 3b and Figure S5) reveal that even smaller nanocrystallite domains exist in the grains, forming a peak size of ∼50 nm in the size distributions (Figure S5). There are many nanosized cracks with widths of ∼1−10 nm lying between the nanocrystallite boundaries (as indicated by the arrows in Figure 3b). High-resolution TEM images further revealed that the nanocrystallites contain many stacking faults (SFs) produced by slipping of lattice planes under external compression (Figure 3c).[38] Similar observations hold for the senary sample (Figure 3d−f). These facts suggest that the applied external high pressure caused abundant nanocracking in the sample grains, which turned the initially micrometer-sized (bulk) sample into nanocrystallites with many SFs.

We performed finer EDS elemental mapping (on an ∼1 μm scale) in the HEB samples before and after compressions to ∼55 GPa to examine possible phase segregation (Figure S6). The results show that all of the metal elements were distributed evenly and no secondary phases were present.

Figure 2a−d shows that there is significant broadening in the XRD peaks with an increase in pressure, which originated from both the nanosizing and microstrain in a sample at high pressure. Hence, the Williamson−Hall analysis[39−41] was used to derive out the average nanocrystallite size and microstrain using the pressure-dependent broadening of XRD peaks having different (*hkl*) indices (Figure S7) after subtraction of the instrumental peak broadening. There are quite high uncertainties in the derived crystallite sizes and microstrains (Figure 3g−j) due to the scattering in the full widths at half-maximum (fwhm) of the two samples (Figure S7), which is likely a consequence of the high hardness of the HEBs that hindered grinding of the samples to form very fine powders for producing ideal diffraction rings (see Figure S2). Even so, it is clear that upon being compressed to ∼5 GPa, the HEB samples started to form nanocracking and nanocrystallites that were ∼50 nm, which remained essentially the same size upon compression to ∼50 GPa and subsequent decompression to ambient pressure (Figure 3g,i). This is in accord with the TEM size statistics shown in panels g and h of Figure S5. The microstrain increases with pressure in general and can be largely relieved upon decompression to ambient pressure (Figure 3h,j). The minor residual microstrain at ambient pressure is due to the nanosizing of the initially micrometer-sized crystallites.

Now it is clear that at high pressure, the quinary or senary HEB sample loaded in a DAC cracked to form nanocrystallites with an average size of ∼50 nm. This small crystallite size triggered the HPL effect[35,42] that enhanced the incompressibility of the HEBs by ∼50−60%, probably through shielding of the external pressure by dynamic dislocation creation and repulsion in the vicinity of the nanocrystallite boundaries.[35,42] This is analogous to the Hall−Petch effect that increases the hardness of small grains via piling and interaction of edge dislocations.[43−45] The high-density SFs in the nanocrystallites can introduce an overlapped strain field and hence also increase the elastic modulus.[46] Ideally, one could further increase the incompressibility by maximizing the Hall−Petch effect via

https://doi.org/10.1021/acs.jpclett.1c00399
J. Phys. Chem. Lett. 2021, 12, 3106−3113

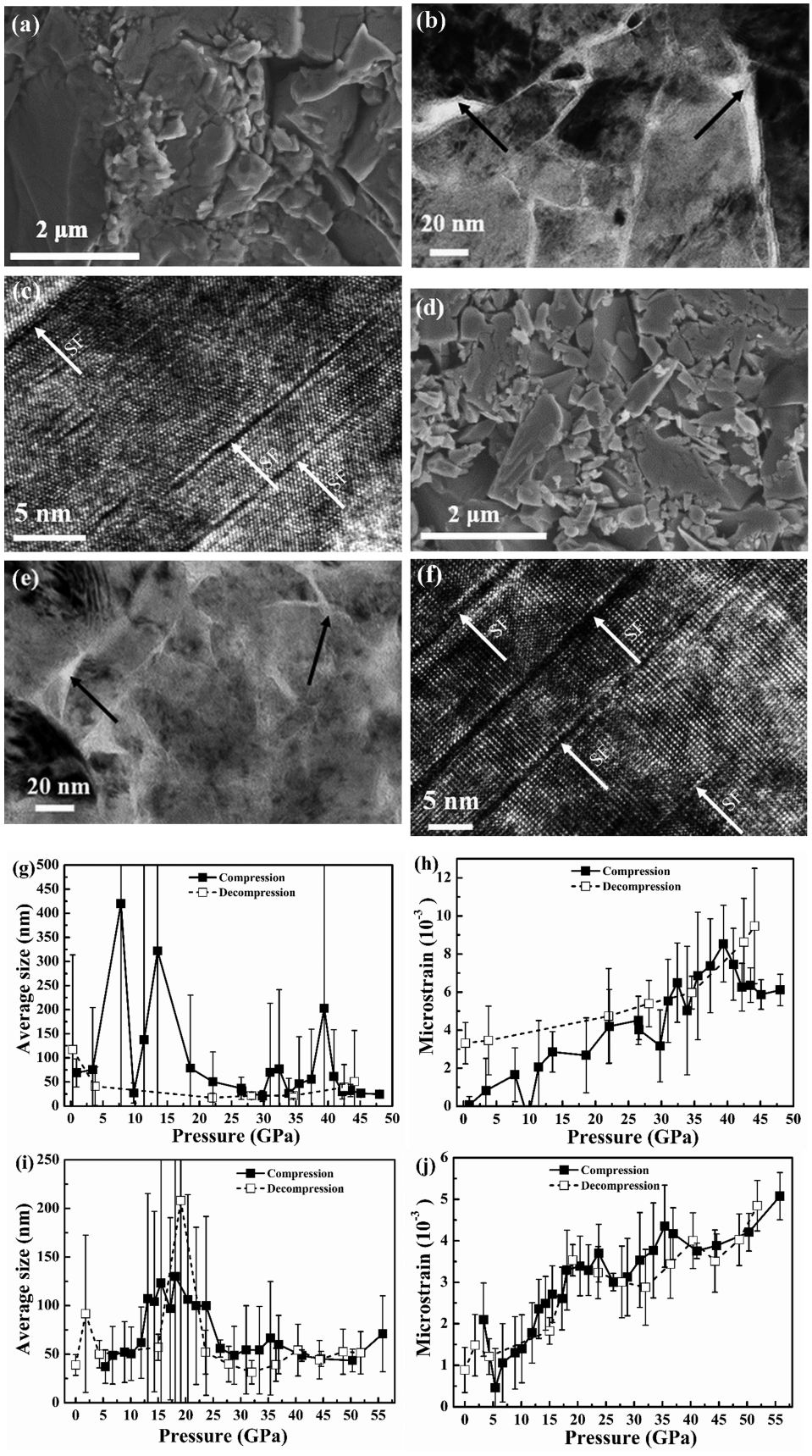

Figure 3. (a) SEM and (b and c) TEM images of the quinary HEB quenched from 55 GPa. (d) SEM and (e and f) TEM images of the senary HEB quenched from 55 GPa. (g) Average grain size of the quinary HEB. (h) Microstrain of the quinary HEB. (i) Average grain size of the senary HEB. (j) Microstrain of the senary HEB. In panels b and e, arrows point to nanocracking; in panels c and f, arrows point to stacking faults (SFs).

https://doi.org/10.1021/acs.jpclett.1c00399
J. Phys. Chem. Lett. 2021, 12, 3106−3113

reducing the nanocrystallite size. However, as shown in panels g and i of Figure 3, the average size of the HP-generated nanocrystallites became rather invariant with pressure, which prevented our attempts.

The experimental bulk moduli of WB_2, OsB_2, and ReB_2 are also significantly higher than the DFT predictions (Table S7). This may also be due to their nanosizing at high pressures, as supported by the low B_0' (1.4) of OsB_2, which is close to the fitted B_0' of our HEBs. On the contrary, the bulk moduli of the constituent simple diborides of the two HEBs are close to the DFT-predicted values (Table S7), suggesting that no nanosizing or SFs were produced in their HP experiments. Thus, we infer that the heterogeneity in the cation chemistry in the HEBs facilitated their nanosizing and SF formation. As atomic heterogeneity is common in all high-entropy compounds and alloys, nanosizing and/or SF formation may be common when they are under HP compression. Thus, our observed enhancement in incompressibility of high-entropy diborides may be common in many HP-compressed high-entropy materials.

In summary, our synchrotron high-pressure XRD study revealed that our two newly synthesized quinary and senary high-entropy diborides are ultra-incompressible, reaching ~90% of that of single-crystal diamond. SEM and TEM imaging and Williamson−Hall size−strain analyses showed that the ultra-incompressibility is due largely to the Hall−Petch-like effect that occurs in nanocrystalline materials, accounting for the 50−60% enhancement of the bulk moduli over those of their bulk counterparts. This work demonstrates a new pathway for producing ultra-incompressible and very hard materials by combining both the "cocktail effect" and Hall−Petch-like effect via nanosizing high-entropy compounds at high pressure.

■ ASSOCIATED CONTENT

Supporting Information

The Supporting Information is available free of charge at https://pubs.acs.org/doi/10.1021/acs.jpclett.1c00399.

Details of experiments and computations, results of XRD, SEM, and EDS, Vickers hardness, nanoindentation hardness, and Young's moduli, high-pressure XRD patterns, relationship between normalized pressure and Eulerian strain, SEM and TEM images and EDS elemental mapping of samples quenched from high pressure, full widths at half-maximum of XRD peaks of samples under compression, cell parameters and unit cell volumes of samples derived from HP-XRD data, and comparisons between the bulk moduli of simple or high-entropy diborides derived from DFT calculations and those obtained from experimental determinations (PDF)

■ AUTHOR INFORMATION

Corresponding Author

Hengzhong Zhang − *Center for High Pressure Science and Technology Advanced Research, Shanghai 201203, China;* orcid.org/0000-0003-2322-2274; Phone: +86-21-80177095; Email: hengzhong.zhang@hpstar.ac.cn

Authors

Xiaoliang Zhang − *Center for High Pressure Science and Technology Advanced Research, Shanghai 201203, China*

Weiwei Li − *Center for High Pressure Science and Technology Advanced Research, Shanghai 201203, China*

Hua Tian − *Center for High Pressure Science and Technology Advanced Research, Shanghai 201203, China*

Junxiu Liu − *Center for High Pressure Science and Technology Advanced Research, Shanghai 201203, China*

Cong Li − *Center for High Pressure Science and Technology Advanced Research, Shanghai 201203, China*

Hongliang Dong − *Center for High Pressure Science and Technology Advanced Research, Shanghai 201203, China; State Key Laboratory of High Performance Ceramics and Superfine Microstructure, Shanghai Institute of Ceramics, Chinese Academy of Sciences, Shanghai 201899, China*

Jian Chen − *Center for High Pressure Science and Technology Advanced Research, Shanghai 201203, China; Department of Physics, Southern University of Science and Technology, Shenzhen, Guangdong 518055, China*

Meng Song − *Center for High Pressure Science and Technology Advanced Research, Shanghai 201203, China*

Bin Chen − *Center for High Pressure Science and Technology Advanced Research, Shanghai 201203, China*

Hongwei Sheng − *Center for High Pressure Science and Technology Advanced Research, Shanghai 201203, China*

Shanmin Wang − *Department of Physics, Southern University of Science and Technology, Shenzhen, Guangdong 518055, China;* orcid.org/0000-0001-7273-2786

Dongzhou Zhang − *Partnership for Extreme Crystallography Program, University of Hawaii at Manoa, Honolulu, Hawaii 96822, United States;* orcid.org/0000-0002-6679-892X

Complete contact information is available at: https://pubs.acs.org/10.1021/acs.jpclett.1c00399

Notes

The authors declare no competing financial interest.

■ ACKNOWLEDGMENTS

This research was supported by the National Natural Science Foundation of China (Grant 21875005). It was also partially supported by the Opening Project of the State Key Laboratory of High Performance Ceramics and Superfine Microstructure (Project SKL201802SIC) and the Research Platform for Crystal Growth & Thin-Film Preparation at SUSTech and the Shenzhen Development and Reform Commission Foundation for Shenzhen Engineering Research Center for Frontier Materials Synthesis at High Pressure. High-pressure synchrotron X-ray diffraction was conducted at beamline station 13-BM-C of the Advanced Photon Source (APS, Lemont, IL). Use of 13-BM-C was supported by COMPRES under National Science Foundation (NSF) Cooperative Agreement EAR-1661511 and by GSECARS through NSF Grant EAR-1634415 and U.S. Department of Energy Grant DE-FG02-94ER14466. The authors thank Yanping Yang (HPSTAR) for assistance with SEM sample characterization.

■ REFERENCES

(1) Akopov, G.; Yeung, M. T.; Kaner, R. B. Rediscovering the crystal chemistry of borides. *Adv. Mater.* **2017**, *29*, 1604506.

(2) Zhou, Y.; Xiang, H.; Feng, Z.; Li, Z. General trends in electronic structure, stability, chemical bonding and mechanical properties of ultrahigh temperature ceramics TMB_2 (TM= transition metal). *J. Mater. Sci. Technol.* **2015**, *31*, 285−294.

(3) Kvashnin, A. G.; Zakaryan, H. A.; Zhao, C.; Duan, Y.; Kvashnina, Y. A.; Xie, C.; Dong, H.; Oganov, A. R. New Tungsten Borides, Their Stability and Outstanding Mechanical Properties. *J. Phys. Chem. Lett.* **2018**, *9*, 3470−3477.

(4) Rost, C. M.; Sachet, E.; Borman, T.; Moballegh, A.; Dickey, E. C.; Hou, D.; Jones, J. L.; Curtarolo, S.; Maria, J. P. Entropy-stabilized oxides. *Nat. Commun.* **2015**, *6*, 8485.
(5) Yalamanchili, K.; Wang, F.; Schramm, I.; Andersson, J.; Johansson Jöesaar, M. P.; Tasnadi, F.; Mücklich, F.; Ghafoor, N.; Odén, M. Exploring the high entropy alloy concept in (AlTiVNbCr)N. *Thin Solid Films* **2017**, *636*, 346−352.
(6) Jin, T.; Sang, X.; Unocic, R. R.; Kinch, R. T.; Liu, X.; Hu, J.; Liu, H.; Dai, S. Mechanochemical-assisted synthesis of high-entropy metal nitride via a soft urea strategy. *Adv. Mater.* **2018**, *30*, 1707512.
(7) Fracchia, M.; Ghigna, P.; Pozzi, T.; Anselmi Tamburini, U.; Colombo, V.; Braglia, L.; Torelli, P. Stabilization by configurational entropy of the Cu(II) active site during CO oxidation on $Mg_{0.2}Co_{0.2}Ni_{0.2}Cu_{0.2}Zn_{0.2}O$. *J. Phys. Chem. Lett.* **2020**, *11* (9), 3589−3593.
(8) Gild, J.; Zhang, Y.; Harrington, T.; Jiang, S.; Hu, T.; Quinn, M. C.; Mellor, W. M.; Zhou, N.; Vecchio, K.; Luo, J. High-entropy metal diborides: A new class of high-entropy materials and a new type of ultrahigh temperature ceramics. *Sci. Rep.* **2016**, *6*, 37946.
(9) Tallarita, G.; Licheri, R.; Garroni, S.; Orru, R.; Cao, G. Novel processing route for the fabrication of bulk high-entropy metal diborides. *Scr. Mater.* **2019**, *158*, 100−104.
(10) Zhang, Y.; Jiang, Z.; Sun, S.; Guo, W.; Chen, Q.; Qiu, J.; Plucknett, K.; Lin, H. Microstructure and mechanical properties of high-entropy borides derived from boro/carbothermal reduction. *J. Eur. Ceram. Soc.* **2019**, *39*, 3920−3924.
(11) Zhang, Y.; Guo, W.-M.; Jiang, Z.-B.; Zhu, Q.-Q.; Sun, S.-K.; You, Y.; Plucknett, K.; Lin, H.-T. Dense high-entropy boride ceramics with ultra-high hardness. *Scr. Mater.* **2019**, *164*, 135−139.
(12) Gild, J.; Wright, A.; Quiambaotomko, K.; Qin, M.; Tomko, J. A.; Shafkat bin Hoque, Md.; Braun, J. L.; Bloomfield, B.; Martinez, D.; Harrington, T.; et al. Thermal conductivity and hardness of three single-phase high-entropy metal diborides fabricated by borocarbothermal reduction and spark plasma sintering. *Ceram. Int.* **2020**, *46*, 6906−6913.
(13) Zhang, Y.; Sun, S.; Zhang, W.; You, Y.; Guo, W.; Chen, Z.; Yuan, J.; Lin, H. Improved densification and hardness of high-entropy diboride ceramics from fine powders synthesized via borothermal reduction process. *Ceram. Int.* **2020**, *46*, 14299−14303.
(14) Tsai, M. H.; Yeh, J. W. High-entropy alloys: a critical review. *Mater. Res. Lett.* **2014**, *2*, 107−123.
(15) Miracle, D. B.; Senkov, O. N. A critical review of high entropy alloys and related concepts. *Acta Mater.* **2017**, *122*, 448−511.
(16) Lönnberg, B. Thermal expansion studies on the group IV-VII transition metal diborides. *J. Less-Common Met.* **1988**, *141*, 145−156.
(17) Sawa, T. Correlation between nanoindentation test result and Vickers hardness. IMEKO TC3, TC5, and TC22 Conference on Metrology in Modern Context, Thailand, November 2010.
(18) Chen, B. Exploring nanomechanics with high-pressure techniques. *Matter Radiat. Extremes* **2020**, *5*, 068104.
(19) Chen, B.; Lutker, K.; Lei, J.; Yan, J.; Yang, S.; Mao, H. K. Detecting grain rotation at the nanoscale. *Proc. Natl. Acad. Sci. U. S. A.* **2014**, *111*, 3350−3353.
(20) Chen, B.; Lutker, K.; Raju, S. V.; Yan, J.; Kanitpanyacharoen, W.; Lei, J.; Yang, S.; Wenk, H. R.; Mao, H. K.; Williams, Q. Texture of nanocrystalline nickel: probing the lower size limit of dislocation activity. *Science* **2012**, *338*, 1448−1451.
(21) Waseda, Y.; Matsubara, E.; Shinoda, K. *X-ray Diffraction Crystallography: Introduction, Examples and Solved Problems*; Springer: Berlin, 2011.
(22) Birch, F. Finite strain isotherm and velocities for single-crystal and polycrystalline NaCl at high pressures and 300 K. *J. Geophys. Res.* **1978**, *83*, 1257−1268.
(23) Mitra, S. *High-Pressure Geochemistry and Mineral Physics: Basics for Planetology and Geo-Material Science*; Elsevier: San Diego, 2004.
(24) Soignard, E.; McMillan, P. F.; Chaplin, T. D.; Farag, S. M.; Bull, C. L.; Somayazulu, M. S.; Leinenweber, K. High-pressure synthesis and study of low-compressibility molybdenum nitride (MoN and MoN_{1-x})-phases. *Phys. Rev. B: Condens. Matter Mater. Phys.* **2003**, *68*, 132101.
(25) Gu, Q.; Krauss, G.; Steurer, W. Transition Metal Borides: Superhard versus Ultra-incompressible. *Adv. Mater.* **2008**, *20*, 3620−3626.
(26) Solozhenko, V. L.; Kurakevych, O. O.; Le Godec, Y. Creation of nanostuctures by extreme conditions: High-pressure synthesis of ultrahard nanocrystalline cubic boron nitride. *Adv. Mater.* **2012**, *24*, 1540−1544.
(27) Cumberland, R. W.; Weinberger, M. B.; Gilman, J. J.; Clark, S. M.; Tolbert, S. H.; Kaner, R. B. Osmium diboride, an ultra-incompressible, hard material. *J. Am. Chem. Soc.* **2005**, *127*, 7264−7265.
(28) Al-Khatatbeh, Y.; Lee, K. From superhard to hard: A review of transition metal dioxides TiO_2, ZrO_2, and HfO_2 hardness. *J. Superhard Mater.* **2014**, *36*, 231−245.
(29) Gražulis, S.; Daškevič, A.; Merkys, A.; Chateigner, D.; Lutterotti, L.; Quiros, M.; Serebryanaya, N. R.; Moeck, P.; Downs, R. T.; Le Bail, A. Crystallography Open Database (COD): an open-access collection of crystal structures and platform for world-wide collaboration. *Nucleic Acids Res.* **2012**, *40*, D420−D427.
(30) Clark, S. J.; Segall, M. D.; Pickard, C. J.; Hasnip, P. J.; Probert, M. I.; Refson, K.; Payne, M. C. First principles methods using CASTEP. *Z. Kristallogr.* **2005**, *220*, 567−570.
(31) Kühne, T. D.; Iannuzzi, M.; Del Ben, M.; Rybkin, V. V.; Seewald, P.; Stein, F.; Laino, T.; Khaliullin, R. Z.; Schütt, O.; Schiffmann, F.; et al. CP2K: An electronic structure and molecular dynamics software package-Quickstep: Efficient and accurate electronic structure calculations. *J. Chem. Phys.* **2020**, *152*, 194103.
(32) Giannozzi, P.; Baroni, S.; Bonini, N.; Calandra, M.; Car, R.; Cavazzoni, C.; Ceresoli, D.; Chiarotti, G. L.; Cococcioni, M.; Dabo, I.; et al. QUANTUM ESPRESSO: a modular and open-source software project for quantum simulations of materials. *J. Phys.: Condens. Matter* **2009**, *21*, 395502.
(33) Jain, A.; Ong, S. P.; Hautier, G.; Chen, W.; Richards, W. D.; Dacek, S.; Cholia, S.; Gunter, D.; Skinner, D.; Ceder, G.; et al. Commentary: The Materials Project: A materials genome approach to accelerating materials innovation. *APL Mater.* **2013**, *1*, 011002.
(34) Andreoni, W.; Yip, S. *Handbook of Materials Modeling Methods: Theory and Modeling*; Springer: Lausanne, Switzerland, 2020.
(35) Chen, B.; Zhang, H.; Dunphy-Guzman, K.; Spagnoli, D.; Kruger, M.; Muthu, D.; Kunz, M.; Fakra, S.; Hu, J.; Guo, Q.; et al. Size-dependent elasticity of nanocrystalline titania. *Phys. Rev. B: Condens. Matter Mater. Phys.* **2009**, *79*, 125406.
(36) El-Awady, J. A. Unravelling the physics of size-dependent dislocation-mediated plasticity. *Nat. Commun.* **2015**, *6*, 5926.
(37) Pande, C.; Cooper, K. Nanomechanics of Hall-Petch relationship in nanocrystalline materials. *Prog. Mater. Sci.* **2009**, *54*, 689−706.
(38) Carrez, P.; Goryaeva, A. M.; Cordier, P. Prediction of mechanical twinning in magnesium silicate post-perovskite. *Sci. Rep.* **2017**, *7*, 17640.
(39) Williamson, G.; Hall, W. X-ray line broadening from filed aluminium and wolfram. *Acta Metall.* **1953**, *1*, 22−31.
(40) Bindu, P.; Thomas, S. Estimation of lattice strain in ZnO nanoparticles: X-ray peak profile analysis. *Int. J. Theor. Phys.* **2014**, *8*, 123−134.
(41) Prabhu, Y. T.; Rao, K. V.; Kumar, V. S. S.; Kumari, B. S. X-ray analysis by Williamson-Hall and size-strain plot methods of ZnO nanoparticles with fuel variation. *World J. Nano Sci. Eng.* **2014**, *2014*, 41004−41012.
(42) Zhou, X.; Feng, Z.; Zhu, L.; Xu, J.; Miyagi, L.; Dong, H.; Sheng, H.; Wang, Y.; Li, Q.; Ma, Y.; et al. High-pressure strengthening in ultrafine-grained metals. *Nature* **2020**, *579*, 67−72.
(43) Hall, E. The deformation and ageing of mild steel: III discussion of results. *Proc. Phys. Soc., London, Sect. B* **1951**, *64*, 747.
(44) Petch, N. The cleavage strength of polycrystals. *J. Iron Steel Inst., London* **1953**, *174*, 25−28.
(45) Naik, S. N.; Walley, S. M. The Hall-Petch and inverse Hall-Petch relations and the hardness of nanocrystalline metals. *J. Mater. Sci.* **2020**, *55*, 2661−2681.
(46) Chen, Y.; Burgess, T.; An, X.; Mai, Y. W.; Tan, H. H.; Zou, J.; Ringer, S. P.; Jagadish, C.; Liao, X. Effect of a high density of stacking

https://doi.org/10.1021/acs.jpclett.1c00399
J. Phys. Chem. Lett. 2021, 12, 3106−3113

faults on the Young's modulus of GaAs nanowires. *Nano Lett.* **2016**, *16*, 1911−1916.

https://doi.org/10.1021/acs.jpclett.1c00399
J. Phys. Chem. Lett. 2021, 12, 3106−3113